High Power Laser Science and Engineering, (2024), Vol. 12, e70, 12 pages.
doi:10.1017/hpl.2024.62

HIGH POWER LASER SCIENCE AND ENGINEERING

RESEARCH ARTICLE

A scintillating fiber imaging spectrometer for active characterization of laser-driven proton beams

J. K. Patel[1,2], C. D. Armstrong[2], R. Wilson[1], M. Alderton[1], E. J. Dolier[1], T. P. Frazer[1], A. Horne[1], A. Lofrese[1], M. Peat[1], M. Woodward[2], B. Zielbauer[3], R. J. Clarke[2], R. Deas[4], P. P. Rajeev[2], R. J. Gray[1], and P. McKenna[1,5]

[1] *SUPA Department of Physics, University of Strathclyde, Glasgow, UK*

[2] *Central Laser Facility, STFC Rutherford Appleton Laboratory, Harwell, Oxford, UK*

[3] *PHELIX Group, GSI Helmholtzzentrum für Schwerionenforschung, Darmstadt, Germany*

[4] *Defence Science and Technology Laboratory, Portsdown West, Fareham, Hampshire, UK*

[5] *The Cockroft Institute, Sci-Tech Daresbury, Warrington, UK*

(Received 17 April 2024; revised 9 August 2024; accepted 11 September 2024)

Abstract

Next generation high-power laser facilities are expected to generate hundreds-of-MeV proton beams and operate at multi-Hz repetition rates, presenting opportunities for medical, industrial and scientific applications requiring bright pulses of energetic ions. Characterizing the spectro-spatial profile of these ions at high repetition rates in the harsh radiation environments created by laser–plasma interactions remains challenging but is paramount for further source development. To address this, we present a compact scintillating fiber imaging spectrometer based on the tomographic reconstruction of proton energy deposition in a layered fiber array. Modeling indicates that spatial resolution of approximately 1 mm and energy resolution of less than 10% at proton energies of more than 20 MeV are readily achievable with existing 100 μm diameter fibers. Measurements with a prototype beam-profile monitor using 500 μm fibers demonstrate active readouts with invulnerability to electromagnetic pulses, and less than 100 Gy sensitivity. The performance of the full instrument concept is explored with Monte Carlo simulations, accurately reconstructing a proton beam with a multiple-component spectro-spatial profile.

Keywords: diagnostics; high repetition rate; ion acceleration; laser–solid interactions

1. Introduction

Laser-driven approaches to ion acceleration have shown promise for applications in medicine, industry and scientific research[1,2], with protons accelerated via target-normal sheath acceleration (TNSA)[3,4] receiving significant attention. Enhancement of proton energies via additional acceleration mechanisms occurring at the onset of relativistic induced transparency has recently been reported, with maximum energies in the 100–150 MeV range[5,6]. The many potential applications of these beams[1,2] mainly require further development of the energy and stability of current laser-driven sources. Measurement of the spatial and spectral profile of these beams is necessary for many applications, and to further investigate the influence of underlying laser–plasma interaction physics on key beam parameters to facilitate continued source development. For example, spatially resolving sub-millimeter-scale features in TNSA proton beams has revealed information about fast electron transport within the target plasma[7–9].

Data-driven methods promise advances across experimentation and analysis[10], which will accelerate the development of laser-driven particle and radiation sources. Development of high-repetition-rate high-power lasers (HPLs), targetry and diagnostics has enabled Bayesian optimization of charge and energy spread stability[11,12] of laser-wakefield accelerated (LWFA) electron beams, and of maximum energies of TNSA protons in simulations[13] and experiments[14]. Active diagnostics that can operate at high repetition rate are essential for capturing large experimental datasets to take advantage of these techniques.

Many studies, particularly involving low-repetition-rate (<1 mHz) lasers, have used stacks of passive detectors

Correspondence to: J. K. Patel, SUPA Department of Physics, University of Strathclyde, Glasgow G4 0NG, UK. Email: jesel.patel@strath.ac.uk

such as radiochromic film (RCF) for spectro-spatial measurements of proton beams[15–17]. RCF stacks are invulnerable to the electromagnetic pulses (EMPs) generated in HPL–plasma interactions[18], and thin ($\lesssim$100 μm) active layers enable high spatial and energy resolution and a compact form factor (~cm) while sampling many (>10) energy bins. However, these detectors are single-shot and require physical removal from the target vacuum chamber for readout, making them unsuitable for online measurements.

Scintillators produce prompt (typically <10 μs) optical pulses at the site of energy deposition by ionizing radiation in their volume[19]. This has given rise to the ubiquity of scintillation-based radiation diagnostics in studies of high-energy-density physics and laser–plasma interactions[20–22]. Proton beam diagnostics based on planar scintillators have been reported, imaged with a charge-coupled device (CCD) or scientific complementary metal–oxide–semiconductor (sCMOS) camera[23–28]. However, the requirement of an optical path along the axis of beam propagation for imaging scintillation light limits the number of discrete energy bins that these methods can resolve. For example, using filter arrays to sample multiple energies within spatial macro-pixels[25–29] results in limited spatial resolution, precluding analysis of fine features that are important in studies of electron transport[7–9] and transient electromagnetic fields[30–34], and imaging applications more generally. An alternative approach uses pinhole projection[35] or bi-telecentric imaging[36] of scintillation light from a scintillator volume. This enables resolution of many energy bins. However, to achieve sufficient sensitivity the optical readout is housed in close proximity to the detector head. The in-chamber electronic readout makes this technique susceptible to interference from the high-amplitude EMPs generated by HPL–plasma interactions[18].

In this paper, we present an approach based on scintillating fibers that generate optical light as protons deposit energy and transport the light away from the axis of proton beam propagation. We extend a recently reported technique for tomographic reconstruction of two-dimensional (2D) X-ray beam profiles[37] to three dimensions for spectro-spatial analysis of laser-driven proton beams. Close packing of small diameter (100 μm) fibers enables spatial resolution of approximately 1 mm, spectral resolution of less than 10% for proton energies of more than 20 MeV and sampling of tens of energy bins in a detector extent of a few centimeters along the beam axis. Optical fibers transport scintillation light away from the laser–plasma interaction with high efficiency, such that subsequent detection is possible with minimal EMP concerns[29]. Imaging the scintillation light from the ends of optical fibers onto a scientific camera allows tuning of the dynamic range via control of the imaging system. An experiment at an HPL facility has been conducted to demonstrate the approach and test the expected sensitivity of a beam-profiler prototype. Geant4[38] Monte Carlo simulations are used to explore the tomographic extension of the technique for three-dimensional (3D) reconstruction of the spectro-spatial profile of a synthetic proton beam. Finally, we discuss this work in the context of diagnostic requirements of high-repetition-rate HPL experiments.

2. Scintillating fiber imaging spectrometer

Scintillating fibers have been established as sensitive detectors in many high-energy-density experiments, such as the LHCb tracker at CERN[20] and for neutron imaging of inertial confinement fusion (ICF) implosions at the National Ignition Facility (NIF)[39], and have been implemented in a profile monitor for ion therapy beams[40]. In Section 2.1 the concept of the scintillating fiber imaging spectrometer (SciFi stack) is introduced and the operating spatial resolution, energy resolution and sensitivity to protons are outlined. Performance is benchmarked against standard use RCF detectors. The design of a beam-profile monitor (BPM) prototype is presented in Section 2.2, which was used to verify the estimated sensitivity of the detector to energy deposited in the scintillating fibers and demonstrate operation at high repetition rates to diagnose laser-accelerated particles.

2.1. Concept and system performance

Figure 1 illustrates the concept of the SciFi stack. An array of parallel scintillating fibers forms a one-dimensional (1D) BPM. The integral of the energy deposited along the length of each fiber, scaled by a factor accounting for ionization quenching[41], is proportional to the output optical signal. The output from fibers in a 1D array corresponds to a projection across the incoming beam. A panel of parallel fibers corresponds to a 1D beam profile at a single Bragg peak energy, assuming gaps between fibers are filled with a material with proton stopping closely matched to the scintillator. Subsequent panels provide profiles at higher energies, according to the relation between a proton's initial energy and its range in the detector volume. By forming a layer of panels at different rotation angles, the combination of 1D projections can be treated as a quasi-sinogram, enabling reconstruction of a 2D beam profile by methods used in emission tomography[42]. By using more panels at more finely spaced angles, the spatial resolution of the system increases whilst sampling a broader energy range.

In general, the spatial resolution of a tomograph is dependent on the particular distribution of the function for which it is the objective to reconstruct, including contrast and noise effects[43], so dedicated studies based on phantoms with standard features are used to compare the performance of different systems. However, the condition that the number of independent samples should match the number of resolved

https://doi.org/10.1017/hpl.2024.62 Published online by Cambridge University Press

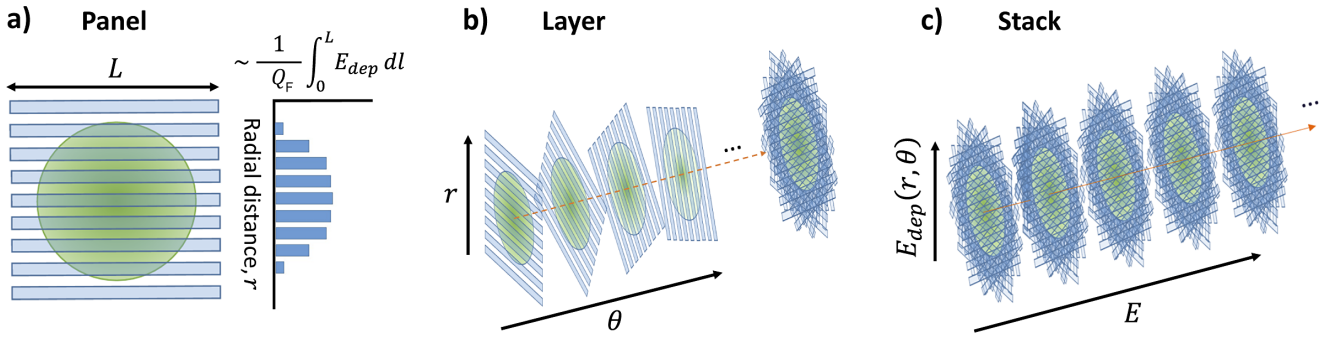

Figure 1. Scintillating fiber imaging spectrometer (SciFi stack) concept. (a) A parallel fiber array forms a single-axis beam-profile monitor. (b) A layer is formed from parallel fiber array panels rotated at a number of angles. This layer samples the 2D beam profile such that it can be reconstructed with tomography methods. (c) Stacking many layers enables reconstruction of many energy bins, maintaining the ability to introduce filtering between the layers to extend the range to high energies in a compact manner.

elements[44,45] can be used to make an initial estimate for our requirements. We can write this condition as follows:

$$n \times m \simeq \frac{\pi R^2}{\delta s^2}, \tag{1}$$

where n is the number of elements in a single projection, m is the number of projection angles, R is the radial size of the sampled area and δs^2 is the area of a resolved element. However, we notice that $\delta s \to 0$ for $m \to \infty$. To enforce the condition that the resolution is limited by the fiber pitch, $\delta s \to 2d_\mathrm{f}$, where d_f is the fiber diameter, we simply add a corrective factor:

$$\delta s \simeq \left(\frac{\pi R}{m} d_\mathrm{f}\right)^{1/2} + 2d_\mathrm{f}. \tag{2}$$

While this has the effect of increasing δs for all m, unaccounted noise and reconstruction artefacts will contribute similarly to the overall resolution, so this is an acceptable estimate. Figure 2(a) shows the spatial resolution of a scintillating fiber tomograph with fiber thicknesses $d_\mathrm{f} = 500, 250, 100$ μm and a typical sampled area radius $R = 25$ mm, compared to published values for the resolution of HDV2 and EBT3 RCFs for 4 MeV protons, using a flat-bed scanner[46]. Resolutions for a benchmark design with $m = 8$ projection angles are labeled, with $\delta s \simeq 3.2, 2.1, 1.2$ mm for the respective fiber thicknesses.

TRIM[47] Monte Carlo simulations allow us to compare the energy resolution of SciFi stack designs to RCF detectors, by approximating the active layer of each as a sub-section in a volume of polystyrene. Here we define dE as the difference between proton energies with a mean range at the maximal and minimal layer depths, and the layer energy, E_mid, as the proton energy with a mean range in the middle of the layer. Figure 2(b) shows the energy resolution of the benchmark SciFi stack designs with active layer thicknesses md_f, and the energy resolution of HDV2 and EBT3 RCFs modeled as 12 and 28 μm active layers of polystyrene, respectively. An upper bound of $\mathrm{d}E/E_\mathrm{mid} = 10\%$ is marked with a black dashed line, and opaque lines are the operating region for each design. The smallest thickness active layer SciFi stack design considered here is 800 μm, compared to RCF active layers less than 100 μm thick. Compared to RCF, the energy resolution of the SciFi stack is therefore inferior at all proton energies; however, a $d_\mathrm{f} = 100$ μm design can resolve proton energies $E_\mathrm{mid} > 20$ MeV with $\mathrm{d}E/E_\mathrm{mid} < 10\%$, and achieve $\delta s \approx 1.2$ mm spatial resolution. While spatial and energy resolution may be improved with $d_\mathrm{f} < 100$ μm fibers (which have been manufactured in fiber bundles[48–50]), there is a trade off with sensitivity. Thinner fibers subtend a smaller solid angle, and the energy deposited by a particle traversing a shorter path will be reduced, so higher flux or more sensitive optical detection is required.

We also note that scintillating fibers with a round cross-section are used in this work due to their more efficient optical transport compared to fibers with square cross-sections. While this choice enhances device sensitivity, round fibers also increase the uncertainty in the detected proton energies within each layer of the SciFi stack. This effect is discussed in more detail in Section 4, where we propose embedding the scintillating fibers in a material with a similar proton stopping power to minimize this uncertainty.

Imaging of scintillation light offers a simple way to readily tune the sensitive range of the detector, via control of the imaging system. Figure 2(c) shows the sensitive range of a SciFi stack as a function of the numerical aperture, *NA*, of the imaging system, using scintillating and optical fiber specifications of the prototype described in Section 2.2 and the specifications of the camera used in the experimental work presented in Section 3. The sensitive range is shown as a green shaded region, bounded by solid and dashed green lines to indicate the noise floor and saturation limit of the imaging system, respectively.

Signals measured by an optical sensor, S [counts], can be expressed as the product of three factors: the energy deposited by protons in a scintillating fiber, E_dep [MeV]; the total efficiency of generation and detection of optical

https://doi.org/10.1017/hpl.2024.62 Published online by Cambridge University Press

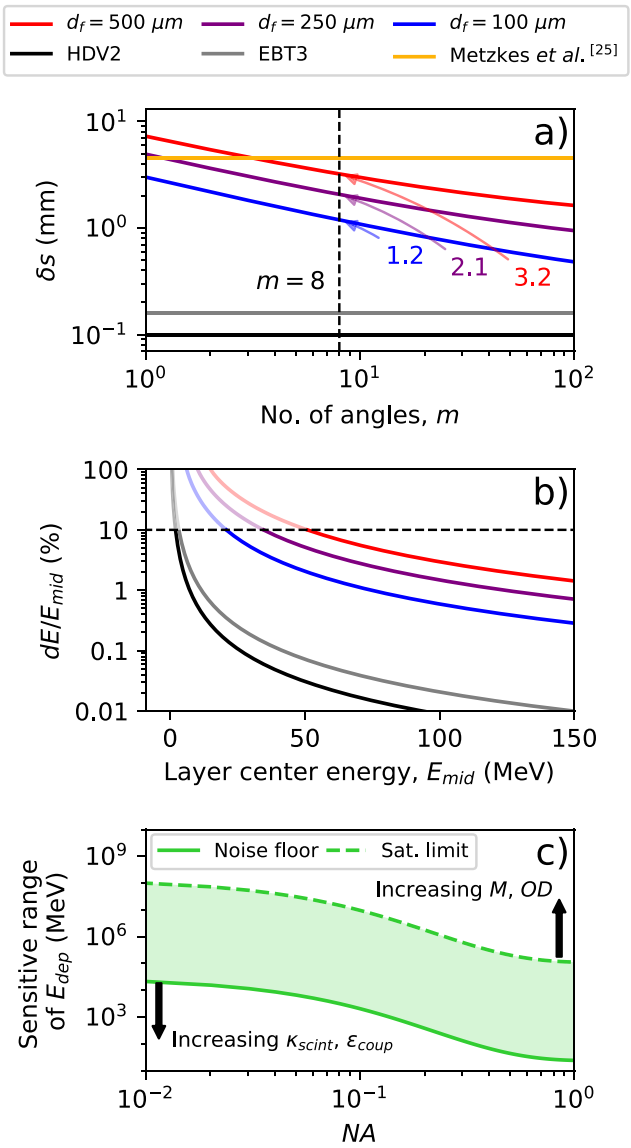

Figure 2. Modeled performance of a SciFi stack imaging spectrometer. (a) Estimated spatial resolution as a function of the number of projection angles, m, for fiber diameters, $d_f = 500, 250, 100$ μm. Resolutions for designs with $m = 8$ angles are labeled. The resolutions of HDV2 and EBT3 RCFs and a plane scintillator instrument with a filter array[25] are shown for comparison. (b) Energy resolution of protons for $m = 8$ SciFi stack designs for each fiber diameter and RCF active layers. (c) Detector sensitive range as a function of the numerical aperture, NA, for $d_f = 500$ μm and the imaging system described in Section 3. The effects of altering the instrument via the magnification, M, or optical density, OD, of the imaging system and scintillation yield, $\kappa_{scint.}$, or fiber coupling efficiency, $\varepsilon_{coup.}$, are indicated with black arrows.

photons in the detector system, $\kappa_{scint}\varepsilon_{fiber}\varepsilon_{lens}\varepsilon_Q/n_{px}$ [photons-per-MeV]; and the optical sensor gain factor, η_{cam} [counts-per-photon]:

$$S = E_{dep} \cdot \frac{\kappa_{scint}\varepsilon_{fiber}\varepsilon_{lens}\varepsilon_Q}{n_{px}} \cdot \eta_{cam}. \quad (3)$$

In the second factor in Equation (3), $\kappa_{scint} = \kappa_{ee}/Q_F$ is the number of optical photons generated per MeV of energy deposited by protons in the scintillator, where $\kappa_{ee} = 7100\ \text{MeV}^{-1}$[51] is the electron equivalent scintillation efficiency and $Q_F = 1.8$ is the ionization quenching correction factor. The quenching factor is determined from the layer-averaged linear energy transfer (LET) found from Monte Carlo simulations (akin to the methods described by Corvino *et al.*[36] and Schollmeier *et al.*[52]) by substituting the LET into the empirical formula for Q_F in polystyrene-based SCSF-3HF fibers[53] in the work of Penner *et al.*[54]. The efficiency of light transport by scintillating and optical fibers is given by $\varepsilon_{fiber} = \varepsilon_{trap.}\varepsilon_{coup.}\varepsilon_{trans.}$, where $\varepsilon_{trap.} = 0.031$ is the fraction of light trapped in the scintillating fiber[53], $\varepsilon_{coup.} = 0.1$ is the fraction coupled to optical transport fibers and $\varepsilon_{trans.} = 0.98$ is the fraction transmitted through the optical fibers[55]. The collection efficiency of the imaging lens is ε_{lens} (see Section 1 of the Supplementary Material), and ε_Q is the quantum efficiency of the camera sensor. The number of pixels over which optical signals are spread is $n_{px} = \pi d_t^2 M^2 / \left(4 s_{px}^2\right)$, where d_t is the diameter of the optical transport fibers, M is the magnification of the imaging system and s_{px} is the sensor pixel pitch. The second and third factors in Equation (3) are the overall sensitivity of the instrument to protons, and thus are fixed by the detector design. The minimum and maximum signals that can be measured are determined by the read noise and the saturation limit of the camera, respectively. Using $S = S_{min}$ and $S = S_{max}$, where S_{min} and S_{max} represent the read noise and saturation limit of the sensor, respectively, Equation (3) can be rearranged to express the sensitive range limits of detector designs in terms of the total energy deposited in a scintillating fiber.

Figure 2(c) shows the sensitive range of the detector as a function of the numerical aperture of the imaging system, and highlights the flexibility of the SciFi stack concept to operate in different environments. Selecting a higher yield scintillator material or increasing the fiber optical coupling efficiency reduces the noise floor of the instrument, as indicated by the downward arrow in Figure 2(c). This sets the lower bound of the sensitive range; however, the final operating region can be selected to suit a particular environment by the choice of the optical sensor and design of the imaging system. Control of the numerical aperture, magnification or optical density of the imaging system can be used for actively tuning the sensitive range of the instrument, enabling characterization over the wide range of source parameters that can be achieved with a single high-repetition-rate HPL system.

2.2. *Beam-profile monitor prototype*

Figure 3 shows a computer-aided design model of the two-axis BPM (SciFi BPM) prototype that has been built and then implemented in laser–solid experiments at the PHELIX[56] and SCAPA[57] laser facilities (see Section 3 in the Supplementary Material for results from the latter). Sixty

https://doi.org/10.1017/hpl.2024.62 Published online by Cambridge University Press

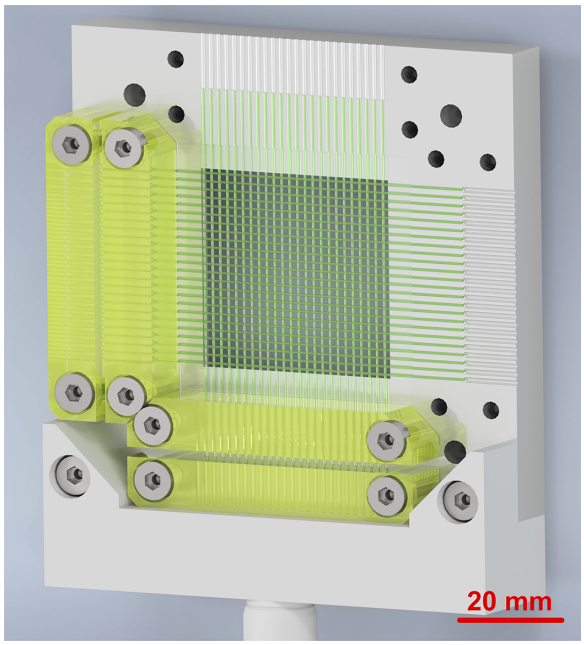

Figure 3. Computer-aided design model render of the SciFi BPM detector head construction, excluding optical transport fibers. Scintillating fibers and fiber clamps are highlighted in green and yellow, respectively. The top and right-hand side fiber clamps have been removed to show the grooves machined in the Al to set the fiber positions.

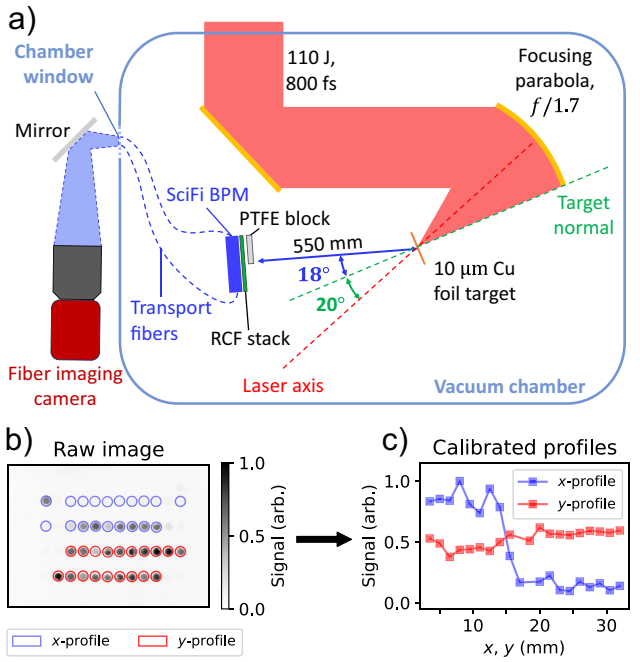

Figure 4. (a) Experimental setup for determination of SciFi BPM sensitivity (not to scale), illustrating the incoming laser path, target and SciFi BPM geometry. A PTFE block is in the path between the target and the SciFi BPM, introducing an edge to the beam, and five layers of RCF are used to absolutely characterize the proton spectrum. Scintillation light from the SciFi BPM travels to the ends of optical transport fibers that are imaged through a window with a camera outside the chamber. (b) Raw image on the SciFi BPM camera. (c) Calibrated SciFi BPM profiles after processing the raw image data.

millimeter lengths of scintillating fibers, Kuraray SCSF-3HF (1500)[53], with diameters $d_f = 500$ μm, are arranged in two perpendicular arrays with a pitch of 1.5 mm. The scintillating fibers are fastened against a machined aluminum frame by 10 mm lengths at the fiber ends with 3D printed clamps. Grooves in the frame and clamps evenly distribute pressure to prevent damage to the delicate fiber cladding. Two meter long, 1 mm diameter plastic optical fibers[55] (not shown in Figure 3) are similarly fastened such that their ends are contact-coupled to each scintillating fiber. Optical fibers carry signals away from the beam axis and output fiber ends are held in a 3D printed structure. Signals are then digitized by imaging onto a complementary metal–oxide–semiconductor (CMOS) camera, and extracted by masking the pixels in the image corresponding to each fiber end. All scintillating and optical transport fiber ends were manually polished with as low as 1 μm grit Al_2O_3 lapping. Emission at the scintillation wavelength ($\lambda = 530$ nm) can also be induced by ultraviolet (UV) excitation, enabling flat-field calibration with a UV light-emitting diode (LED) ($\lambda = 380$ nm), described in more detail in Section 2 in the Supplementary Material. By illuminating individual fibers with the UV LED, this method was also used to measure a maximum optical cross-talk of 10^{-3} between fibers.

3. Experimental results

Two experiments have been conducted with 100 TW-class laser pulses incident to tens-of-micrometers thick solid targets, in two pulse duration regimes. In this section RCF measurements of TNSA protons accelerated by the approximately 800 ps PHELIX laser are used to benchmark the sensitivity of the SciFi BPM, and demonstrate the capability to resolve spatial variations introduced to the proton beam, using an active readout capable of high-repetition operation. Results obtained using the approximately 30 fs SCAPA laser are presented in Section 3 in the Supplementary Material, where the SciFi BPM was used to diagnose laser–solid interactions at laser-limited repetition rates of more than 0.01 Hz, with Monte Carlo numerical simulations used to analyze the species and energy distribution of the measured particles.

Figure 4(a) shows the experimental geometry used to determine the sensitivity of the BPM and capability to spatially diagnose proton beams at the PHELIX laser facility. A laser pulse with energy $E_L = (110 \pm 10)$ J and pulse duration $\tau_L = (800 \pm 100)$ fs was incident on a 10 μm thick Cu foil, focused to a spot radius of $r = (20 \pm 2)$ μm by displacing the foil by approximately 90 μm relative to the best focus, yielding an intensity of $I_L = (1.1 \pm 0.3) \times 10^{19}$ W cm^{-2} using uncertainties for E_L, τ_L and r based on compressor-throughput calorimetry, autocorrelator measurements and low-power focal spot image analysis, respectively.

The SciFi BPM is positioned in the direction of the beam of protons accelerated from the target rear, at 18° from target

https://doi.org/10.1017/hpl.2024.62 Published online by Cambridge University Press

normal and 550 mm away from the target. Typical proton beam divergence of more than 10° ensures small variations in the beam profile are smoothed out at this distance, and a laminar portion of the beam is sampled. A 5 mm thick polytetrafluoroethylene (PTFE) block that will stop protons up to $E \approx 23$ MeV is placed in the beam to introduce an edge feature, and five layers of HDV2 RCF are placed before the SciFi BPM to provide absolute characterization of the incident proton beam. A 13 μm thick Al foil before the RCF stops heavier ions (e.g., carbon and oxygen) in the energy range produced in the experiment and protons with energy of less than 0.9 MeV, and is also used between the final RCF layer and the SciFi BPM to provide light tightening of the scintillating fibers. One end of each scintillating fiber is coupled to transport fibers in this case, and the transport fiber ends are imaged through a chamber window with an $f/2.5$ lens at a working distance $d_W \approx 1.2$ m, ensuring effective invulnerability to EMPs. An AVT Manta G-235B[58] with a Sony IMX174 CMOS sensor was used in this setup. The collection efficiency by lens imaged emission from round, single-clad optical fibers is dependent on the exit angle from the fiber and the subtended angle of the lens. The derivation of the collection efficiency is given in Section 1 in the Supplementary Material. For this long working distance setup the lens collection efficiency is 0.06%.

Calibrated RCF signals and SciFi BPM data are presented in Figure 5. The number of protons detected in the five layers of HDV2 RCF is shown in Figure 5(a), where the RCF was scanned with a Nikon Super CoolScan 9000 and calibrated in comparison to scans of HDV2 films exposed to known doses at the Birmingham MC40 cyclotron[59]. This calibration is used to convert scanned signals to the energy deposited in each RCF. By normalizing the energy deposited to the Bragg peak energy of the RCF layer, its full width at half maximum (FWHM), dE, and the solid angle subtended by the area of the scanned RCF pixels, dΩ, we derive the proton flux in units of MeV^{-1} sr^{-1}. This quantity remains independent of the detector configuration, allowing for straightforward comparisons with other studies. Regions of interest (ROIs) associated with the scintillating fibers in the BPM behind the RCF are overlaid as green and yellow lines. Blue markers in Figure 5(b) show the calibrated RCF signals summed over the horizontal fiber ROI corresponding to the scintillating fiber with the highest signal in the flat-field calibration, henceforth denoted by the subscript, α, and indicated in Figure 5(a) with the yellow line. Fiber α has the highest optical throughput of all the coupled fibers, and therefore the lowest signal uncertainty resulting from shot noise. RCF signals in the fiber α ROI are plotted at the Bragg peak energies found with TRIM Monte Carlo simulations. Error bars indicate the FWHM of the Bragg peaks. An isothermal plasma expansion model introduced by Mora[60] for TNSA proton spectra is used to predict the proton spectrum incident to the scintillating fibers, given here for convenience in Equation (4):

$$\frac{\mathrm{d}N}{\mathrm{d}E} = \frac{N_0}{\sqrt{2Ek_\mathrm{B}T_\mathrm{e}}} \exp\left(-\sqrt{\frac{2E}{k_\mathrm{B}T_\mathrm{e}}}\right), \tag{4}$$

where N_0 is the total number of accelerated protons, E is the proton energy, k_B is the Boltzmann constant and T_e is the hot electron temperature. A maximum energy cutoff is given by the following:

$$E_\mathrm{max} = 2k_\mathrm{B}T_\mathrm{e}\left(\ln\left(t_\mathrm{p} + \sqrt{t_\mathrm{p}^2+1}\right)\right)^2, \tag{5}$$

where $t_\mathrm{p} = 1.3\tau_\mathrm{L}\omega_\mathrm{pi}/\sqrt{2\exp(1)}$ is the normalized acceleration time[61], using ion plasma frequency $\omega_\mathrm{pi} = \sqrt{e^2 n_{e0}/m_\mathrm{p}\varepsilon_0}$ for protons with mass, m_p, initial electron density, n_{e0}, and vacuum permittivity, ε_0. Established scaling laws[62,63] are in agreement at $I_\mathrm{L} \approx 10^{19}$ W cm^{-2}, and can be used to estimate a hot electron temperature of $k_\mathrm{B}T_\mathrm{e} \approx 0.65$ MeV. Equation (5) then gives a proton cutoff energy of 20.3 MeV. Using $E_\mathrm{max} = 20.3$ MeV, the hot electron temperature $k_\mathrm{B}T_\mathrm{e} = 0.83$ MeV is obtained by fitting Equation (4) to the RCF data. Any choice of $E_\mathrm{max} > 10$ MeV is found to result in a less than 1% change in the value obtained for $k_\mathrm{B}T_\mathrm{e}$, ensuring confidence in the validity of the fit.

Monte Carlo simulations provide the energy deposited per proton in five RCF active layers and two 500 μm layers of polystyrene as a function of proton energy, where the latter layers are used to model the two layers of scintillating fibers. These deposition profiles for the RCF active layers and the scintillating fiber layers are shown in Figure 5(b) with blue and green solid lines, respectively, after being scaled by the proton spectrum incident on fiber α, $\frac{\mathrm{d}N_\alpha}{\mathrm{d}E\mathrm{d}\Omega}$. The second layer of scintillating fibers is exposed to a portion of the beam that has traversed only the RCF layers, due to the gaps between the fibers in the first layer, as well as a portion that has traversed the additional material of the first layer of fibers. To account for the change in the response due to attenuation by the first layer, the response of the second layer of fibers can be expressed as the sum of two components. The energy deposited in the second layer is as follows:

$$E_\mathrm{dep,L2} = \frac{A_1E_\mathrm{T1} + A_2E_\mathrm{T2}}{A_\mathrm{tot.}}, \tag{6}$$

where E_T1 and E_T2 are the energy deposition in monolithic layers 1 and 2, respectively, A_1 and A_2 are the areas of the scintillating fibers in the second SciFi BPM layer of vertically oriented fibers that are exposed to the equivalent filtering of monolithic layers 1 and 2, respectively, and $A_\mathrm{tot.}$ is the total area of the vertical fibers exposed to the beam. The dark green line in Figure 5(b) shows the response of the second layer multiplied by the proton spectrum incident to

https://doi.org/10.1017/hpl.2024.62 Published online by Cambridge University Press

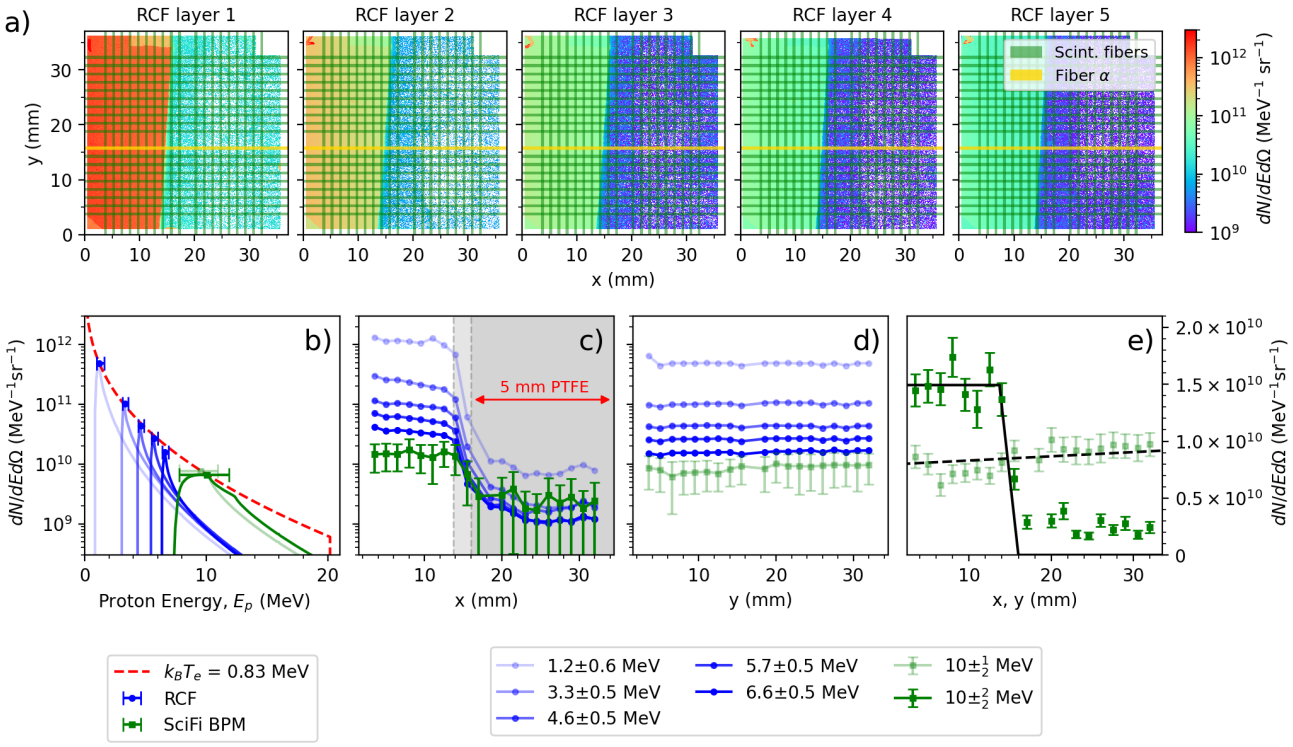

Figure 5. Calibrated RCF and SciFi BPM data for measuring sensitivity and verifying the spatial capability of the detector. (a) Scanned RCF from the front of the SciFi BPM. Green lines indicate positions of scintillating fibers in the BPM behind the RCF layers, used as ROIs for comparison to fiber signals. The yellow line is the ROI for fiber α. (b) Proton spectrum for fiber α. Blue markers are the RCF summed signals in the fiber ROI, at the Bragg peak energies of each RCF layer found with Monte Carlo simulations and labeled in the lower right-hand legend. The dashed red line is the proton spectrum from Equation (4) fit to the RCF data, with $E_{\max} = 20.3$ MeV. Solid blue and green lines are the simulation proton deposition for RCF layers and 0.5 mm scintillating fibers, respectively, scaled by the fitted spectrum. Green markers are the predicted deposition in the scintillating fibers. Error bars are the full width at half maximum (FWHM) of the Bragg peaks. (c) Horizontal and (d) vertical profiles from RCF fiber ROIs (blue) and calibrated SciFi BPM signals (green). See the main text for discussion of uncertainty limits. The darker grey shaded region in (c) shows positions where the whole length of fibers is blocked by PTFE, and the lighter grey region indicates fibers that are partially blocked due to the angle of the filter from vertical. (e) SciFi horizontal (dark green) and vertical (light green) profiles on a linear y-scale. Black solid and dashed lines are idealized proton x- and y-profiles, respectively, with the filter modeled as a binary mask rotated at $\phi = 3.7°$ to the vertical.

fiber α:

$$E_{\text{dep,L2}} \frac{\mathrm{d}N_\alpha}{\mathrm{d}E\mathrm{d}\Omega}.$$

The energy deposited in scintillating fiber α is as follows:

$$E_{\text{dep},\alpha} = E_{\text{BP}} \iint E_{\text{T1}} \frac{\mathrm{d}N_\alpha}{\mathrm{d}E\mathrm{d}\Omega} \mathrm{d}E\mathrm{d}\Omega, \tag{7}$$

where E_{BP} is the Bragg peak energy, and the integrand is shown with the pale green line in Figure 5(b). Taking the ratio of the measured signal to the deposited energy yields the detector sensitivity for fiber α: $\xi_\alpha = S_\alpha / E_{\text{dep}}$. This is equivalent to the product of the second and third factors in Equation (3). The range of energies deposited in the scintillating fibers to which the instrument is sensitive is thus obtained by dividing the camera noise floor and saturation limit each by ξ_α, yielding a sensitive range of 49 GeV–230 TeV for this long working distance imaging system. For a 500 μm diameter polystyrene scintillating fiber with a 35 mm length exposed to the beam, this is equivalent to 80 Gy–3.8 MGy absorbed dose. Scaling the flat-frame calibration obtained with a UV LED by ε_α provides a cross-calibration for the energy deposited in all fibers. Accounting again for the Bragg peak energy of the fiber, E, the FWHM, $\mathrm{d}E$, and the solid angle subtended by the fibers, $\mathrm{d}\Omega$, we obtain the horizontal and vertical profiles shown in Figures 5(c) and 5(d) with dark green and light green markers, respectively. RCF signals obtained by summing over the fiber ROIs are also shown in blue. Error bars in the SciFi BPM profiles are calculated by treating the signals from the UV flat-field calibration and the measurement of laser-accelerated protons as Poisson processes, with uncertainties $\delta = \sqrt{N_{\text{p}}}$, where N_{p} is the equivalent number of protons with energies within the FWHM of the Bragg peak of the layer.

Dark green symbols in Figure 5(e) show the clear edge in the horizontal SciFi profile on a linear y-scale, with a contrast ratio of $\left(I_{\text{sig.}} - I_{\text{bkg.}}\right) / \left(I_{\text{sig.}} + I_{\text{bkg.}}\right) = 0.7$, where $I_{\text{sig.}}$ is the mean of the signals in fibers to the left of the edge in the profile ($x < 13.7$ mm), and $I_{\text{bkg.}}$ is the mean of the signals in fibers to the right of the edge ($x > 16$ mm). Black solid and dashed lines are idealized proton x- and y-profiles, respectively, normalized to $I_{\text{sig.}}$. These are obtained by modeling the filter as a binary mask rotated

https://doi.org/10.1017/hpl.2024.62 Published online by Cambridge University Press

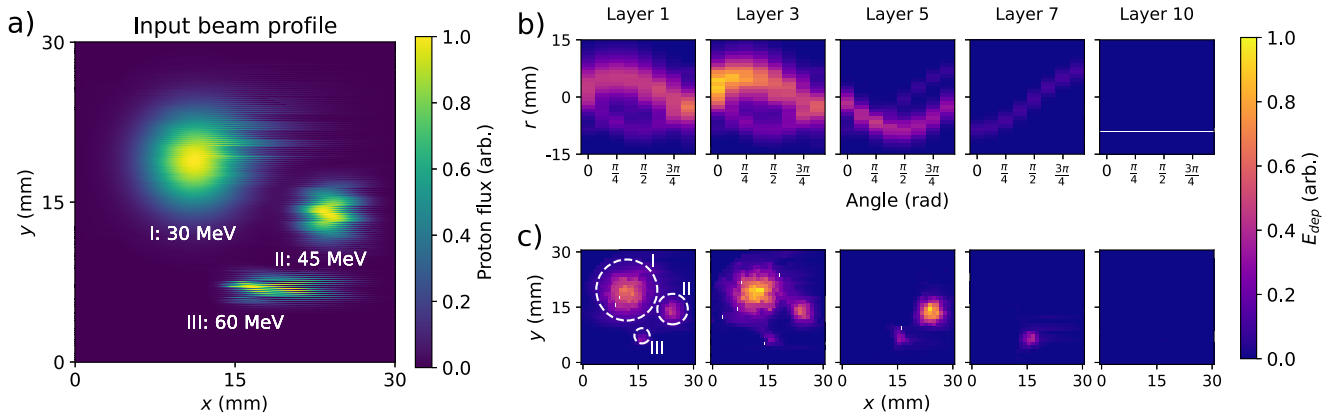

Figure 6. (a) Proton beam profile used for Geant4 simulations. (b) Sinograms generated from selected layers of the SciFi stack. (c) MLEM reconstructions of the energy deposited in the selected SciFi stack layers. Regions of interest with a radius of $2\sigma_{\text{beam}}$ are used for evaluating the reconstructed energy deposited by each beamlet, and are shown with white dashed lines.

at $\phi = 3.7°$ to the vertical, and assuming the filter blocks all protons. The gradient of the step in the x-profile and the overall gradient in the y-profile are therefore entirely determined by the rotation angle of the filter edge. Good agreement between the modeled and the measured profiles demonstrates the potential of the technique for diagnosing subtle spatial variation in laser-accelerated proton beams.

4. Three-dimensional SciFi stack: Monte Carlo simulations

To demonstrate the extension of the simple two-axis BPM design to the full tomographic imaging spectrometer illustrated in Figure 1, the SciFi stack concept was modeled using Geant4. Each panel of parallel fibers is modeled as thirty 30 mm long, 500 μm diameter polystyrene cylinders with a 1 mm pitch. A 2D tomographic layer is formed from eight panels of fibers rotated at 22.5° intervals and separated by 0.2 mm. Ten such tomographic layers separated by 2 mm thick PTFE filters are then stacked to enable spectral analysis, with no filtering before the first layer. To benchmark the spatial and spectral performance of the instrument, a proton beam with a triple-Gaussian spatial structure (see Figure 6(a)) is incident on the detector array. The simulated Gaussian beamlets have radii (at one standard deviation, σ_{beam}) $r_{\text{beam}} = 4, 2, 1$ mm, and have monoenergetic energy spectra at $E_0 = 30, 45, 60$ MeV. Fiber signals are retrieved by integrating the energy deposited in each fiber volume and arranging the signals from each layer into a sinogram. Each sinogram is then processed by a maximum-likelihood expectation maximization (MLEM)[64] algorithm to reconstruct a 2D profile of the energy deposited.

A selection of the sinograms and reconstructed profiles for five tomographic layers is shown in Figures 6(b) and 6(c), respectively, demonstrating the capability to spatially resolve all three of the Gaussian beamlets in layers 1–3. Beamlet I has increasing energy deposition from layers 1–3, but is not observed in the later layers. Beamlets II and III penetrate to deeper layers according to their higher proton energies, in both the reconstructions and the corresponding sine-wave features in the sinograms. The total energy deposited in each layer is plotted as a function of the effective depth of plastic traversed with black markers in Figure 7, with layers whose sinograms and reconstructions are plotted in Figures 6(b) and 6(c) highlighted with yellow circles. To account for the gaps between fibers, the effective depth of polystyrene is calculated for each layer as the average depth of polystyrene traversed by protons in the middle of each layer. The depth of the PTFE filters is added between each layer of fibers to calculate the total effective depth of plastic traversed. The error bars in Figure 7 are the upper and lower limits of the effective depth of each fiber layer. Three distinct step-like features are clearly observed in the total deposition-depth profile. The spatial reconstructions enable us to evaluate the reconstructed signal in ROIs corresponding to each of the beamlets (dashed white lines in Figure 6(c)). These are plotted for beamlets I–III with blue, purple and red symbols, respectively. The deposition-depth profile of each beamlet clearly corresponds to each of the step-features in the total layer profile, and exhibits a Bragg-peak-like shape characteristic of monoenergetic proton deposition. A second peak in the depth-deposition profile for beamlet I, at a depth of approximately 32 mm, is beyond the range of 35 MeV protons in polystyrene. On inspection of the reconstructions at these greater depths, this feature is found to be an artefact resulting from the sparse angular sampling of the beam profile, used to limit the depth of each layer and the corresponding range of energies that are sampled. Future work will investigate the application of reported interpolation methods[65] to mitigate these artefacts.

The Bragg peak deposition that is evident from the data shown in Figure 7 enables the application of iterative algorithms to accurately reconstruct energy distributions. For example, the spatial distribution of the highest energy protons can be measured in the last layer with signals above the background noise, and subtracted from earlier layers to

https://doi.org/10.1017/hpl.2024.62 Published online by Cambridge University Press

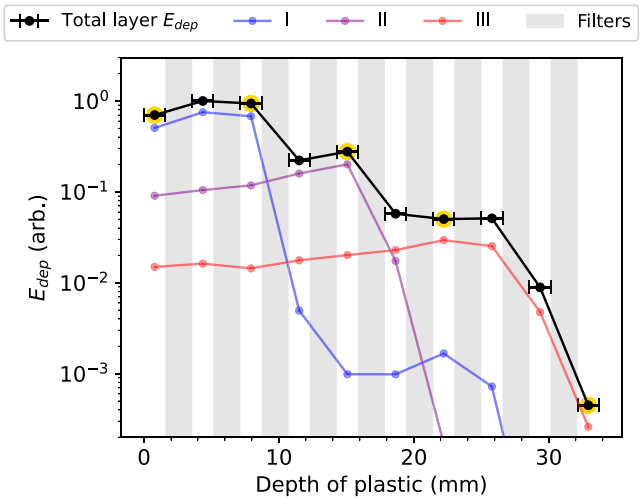

Figure 7. Energy deposition as a function of depth of plastic. Black symbols show the total energy deposition in each layer, where gold circles highlight the layers whose spatial reconstructions are plotted in Figure 6(c). Blue, purple and red symbols are the reconstructed energy deposition within the regions of interest for beamlets I–III, respectively. The grey shaded regions indicate the 2 mm thick filters between the scintillating fiber layers.

isolate the deposition from lower energy protons[66]. While ionization quenching will suppress scintillation at the Bragg peak, existing analysis methods[52] can be implemented to account for this in the spectral reconstruction.

Gaps between fibers result in a complex deposition profile, preventing straightforward reconstruction of the energy spectrum. The fixed arrangement of fibers in each layer results in some paths through the diagnostic intersecting significantly more fiber volume than others, causing a spatially dependent attenuation of the beam profile and degrading the energy resolution of layers deeper in the stack. Fibers with round cross-sections, chosen in this work for their efficient optical transport, also exhibit the characteristic that protons that traverse the center of a fiber are attenuated more than those that traverse the edge. This differential attenuation contributes to increased uncertainty in the energy of the protons detected by fibers at a specific depth in the detector. Embedding the scintillating fibers in a polymer of similar density to the fiber material could mitigate these effects, facilitating spectral reconstruction using established techniques[15,67]. Using a polymer that strongly absorbs light at the scintillation wavelength would further prevent any potential increase in optical cross-talk between fibers. The full spectro-spatial reconstruction using this approach will therefore be demonstrated in future work.

In the simulation results presented here, the proton beamlets were implemented with idealized parameters, including zero divergence angle, to demonstrate the main capability to diagnose spatial and energy features in proton beams. However, proton beams from laser–foil interactions have divergence angles of tens of degrees, and the divergence also varies with proton energy[15,16]. Subsequent panels within tomograph layers will therefore sample spatial distributions that change by a small amount, potentially causing aberrations in the reconstructed profiles and reducing spatial resolution. To address this, a smaller number of panels could be used to analyze narrower energy bands than a full tomograph layer, for example with $m = 8$ panels. Using fewer angular samples will result in lower resolution spatial reconstructions, but may be sufficient to ascertain a key beam parameter, such as the diameter of a beam. By using a smaller number of panels, the beam diameter can be measured throughout the depth of the scintillating fiber stack by scanning panel by panel. The energy dependence of the divergence of the beam can thus be characterized. The variation of the apparent size of the beam measured by each panel can then be compensated to mitigate aberrations in the reconstruction. Future work will evaluate the proposed analysis methods with broadband energy spectra and spatial beam profiles, which are more representative of those expected from laser–plasma interactions, and will characterize the spatial resolution of the instrument in more detail.

5. Summary

In studies at single-shot HPL systems, RCF has proven to be an important diagnostic of spectro-spatial distribution of laser-accelerated protons. However, the increasing prevalence of high-repetition-rate HPL systems requires the development of active detection systems that can operate at matching repetition rates. The SciFi stack imaging spectrometer is introduced to address this.

A stack-style design similar to RCF diagnostics enables a compact form factor, with optical transport away from the beam axis removing the requirement of an axial optical path required by imaging systems in previous approaches[23–26,28]. High sensitivity has been demonstrated with a prototype BPM, taking advantage of the volume integration of energy deposited in scintillating fibers in measured optical signals. Electrons from laser–solid interactions have also been measured in a short working distance setup, with a laser pulse energy of a few joules. The results from this work are presented in Section 3 of the Supplementary Material. Analytical modeling suggests that the sensitivity of the SciFi BPM prototype, equipped with 500 μm diameter fibers, could be enhanced for detecting deposited energies below 100 MeV by directly coupling transport fibers to optical sensors. This approach could also be extended to measure hard X-rays for studies involving betatron radiation[68] or inverse Compton scattering[69–71], for example. There are established routines for deconvolving the spectra of hard X-rays using attenuating detectors[72–75], and a similar technique applied to 2D dose reconstruction for quality assurance of clinical X-ray beams was recently reported[37].

Efficient optical fiber transport of scintillation light enables long working distance imaging, with readout electronics located at large distances from interactions,

https://doi.org/10.1017/hpl.2024.62 Published online by Cambridge University Press

making EMP mitigation straightforward. Imaging of transported optical signals offers readily tuned sensitive range, via control of numerical aperture, magnification or optical density. Energy resolution of less than 10% at proton energies more than 20 MeV and spatial resolution of approximately 1 mm is attainable with 100 μm diameter scintillating fibers, which can be achieved with current manufacturing capabilities.

In the work presented in Section 3 of the Supplementary Material we demonstrate operation at repetition rates of up to 0.05 Hz using the SCAPA laser system[57]. This capability facilitated measurements with reduced uncertainty and enabled quantitative comparison of the relative fluence of protons and electrons by comparing the measurements against numerical simulations. Moreover, the instrument's sensitivity is such that it can function as a single-shot diagnostic in finely sampled parameter scans or efficiently explore the high-dimensional parameter space of laser–solid interactions. The SciFi imaging spectrometer is ultimately capable of camera readout rates exceeding 100 Hz[76], positioning it for the future of data-driven experiments in the next generation of HPL facilities that are expected to operate at high repetition rates.

The results presented in Section 3 of the Supplementary Material also indicate that ionization quenching in plastic scintillators with thicker active layers than RCF suggests that electrons are likely a significant source of background signal when diagnosing ions from laser–solid interactions. However, recent developments have introduced automated segmentation methods to distinguish contributions from different species in RCF stack analysis[77]. These methods can also be applied to spectro-spatial profiles from a SciFi stack diagnostic to distinguish between contributions from electrons and protons to measured profiles. This capability highlights the versatility of the proposed technique in diagnosing multiple particle species.

Further Monte Carlo simulations will be conducted in future work to characterize the spatial resolution of SciFi stack designs, to investigate the impact of beam divergence on reconstructions and evaluate analysis methods with a range of spectro-spatial beam profiles relevant to laser–plasma experiments.

Acknowledgements

The authors gratefully acknowledge the expertise of the PHELIX laser staff at the GSI laboratory, the SCAPA facility staff at the University of Strathclyde and support from the engineering and target fabrication staff at the Central Laser Facility. The results presented in Section 3 are based on experiment P215, which was performed at PHELIX at the GSI Helmholtzzentrum für Schwerionenforschung, Darmstadt, Germany, in the context of FAIR Phase-0. This work is financially supported by STFC, Dstl and EPSRC (grant numbers EP/R006202/1, EP/V049232/1 and EP/P020607/1) and by Laserlab-Europe (grant agreement number 871124, European Union's Horizon 2020 research and innovation program).

Supplementary material

The supplementary material for this article can be found at https://doi.org/10.1017/hpl.2024.62.

Data availability statement

The data associated with research published in this paper are publicly available, and can be accessed at https://edata.stfc.ac.uk/handle/edata/964.

References

1. H. Daido, M. Nishiuchi, and A. S. Pirozhkov, Rep. Prog. Phys. **75**, 056401 (2012).
2. A. Macchi, M. Borghesi, and M. Passoni, Rev. Mod. Phys. **85**, 751 (2013).
3. E. L. Clark, K. Krushelnick, J. R. Davies, M. Zepf, M. Tatarakis, F. N. Beg, A. Machacek, P. A. Norreys, M. I. K. Santala, I. Watts, and A. E. Dangor, Phys. Rev. Lett. **84**, 670 (2000).
4. S. C. Wilks, A. B. Langdon, T. E. Cowan, M. Roth, M. Singh, S. Hatchett, M. H. Key, D. Pennington, A. MacKinnon, and R. A. Snavely, Phys. Plasmas **8**, 542 (2001).
5. A. Higginson, R. J. Gray, M. King, R. J. Dance, S. D. R. Williamson, N. M. H. Butler, R. Wilson, R. Capdessus, C. D. Armstrong, J. S. Green, S. J. Hawkes, P. Martin, W. Q. Wei, S. R. Mirfayzi, X. H. Yuan, S. Kar, M. Borghesi, R. J. Clarke, D. Neely, and P. McKenna, Nat. Commun. **9**, 724 (2018).
6. T. Ziegler, I. Göthel, S. Assenbaum, C. Bernert, F.-E. Brack, T. E. Cowan, N. P. Dover, L. Gaus, T. Kluge, S. Kraft, F. Kroll, J. Metzkes-Ng, M. Nishiuchi, I. Prencipe, T. Püschel, M. Rehwald, M. Reimold, H.-P. Schlenvoigt, M. E. P. Umlandt, M. Vescovi, U. Schramm, and K. Zeil, Nat. Phys. **20**, 1211 (2024).
7. J. Fuchs, T. E. Cowan, P. Audebert, H. Ruhl, L. Gremillet, A. Kemp, M. Allen, A. Blazevic, J.-C. Gauthier, M. Geissel, M. Hegelich, S. Karsch, P. Parks, M. Roth, Y. Sentoku, R. Stephens, and E. M. Campbell, Phys. Rev. Lett. **91**, 255002 (2003).
8. P. McKenna, A. P. L. Robinson, D. Neely, M. P. Desjarlais, D. C. Carroll, M. N. Quinn, X. H. Yuan, C. M. Brenner, M. Burza, M. Coury, P. Gallegos, R. J. Gray, K. L. Lancaster, Y. T. Li, X. X. Lin, O. Tresca, and C.-G. Wahlström, Phys. Rev. Lett. **106**, 185004 (2011).
9. D. A. MacLellan, D. C. Carroll, R. J. Gray, N. Booth, M. Burza, M. P. Desjarlais, F. Du, B. Gonzalez-Izquierdo, D. Neely, H. W. Powell, A. P. L. Robinson, D. R. Rusby, G. G. Scott, X. H. Yuan, C.-G. Wahlström, and P. McKenna, Phys. Rev. Lett. **111**, 095001 (2013).
10. A. Döpp, C. Eberle, S. Howard, F. Irshad, J. Lin, and M. Streeter, High Power Laser Sci. Eng. **11**, e55 (2023).
11. R. J. Shalloo, S. J. D. Dann, J. N. Gruse, C. I. D. Underwood, A. F. Antoine, C. Arran, M. Backhouse, C. D. Baird, M. D. Balcazar, N. Bourgeois, J. A. Cardarelli, P. Hatfield, J. Kang, K. Krushelnick, S. P. D. Mangles, C. D. Murphy, N. Lu, J. Osterhoff, K. Põder, P. P. Rajeev, C. P. Ridgers, S. Rozario, M. P. Selwood, A. J. Shahani, D. R. Symes, A. G. R. Thomas, C.

Thornton, Z. Najmudin, and M. J. V. Streeter, Nat. Commun. **11**, 6355 (2020).
12. S. Jalas, M. Kirchen, P. Messner, P. Winkler, L. Hübner, J. Dirkwinkel, M. Schnepp, R. Lehe, and A. R. Maier, Phys. Rev. Lett. **126**, 104801 (2021).
13. E. J. Dolier, M. King, R. Wilson, R. J. Gray, and P. McKenna, New J. Phys. **24**, 073025 (2022).
14. B. Loughran, M. J. V. Streeter, H. Ahmed, S. Astbury, M. Balcazar, M. Borghesi, N. Bourgeois, C. B. Curry, S. J. D. Dann, S. DiIorio, N. P. Dover, T. Dzelzainis, O. C. Ettlinger, M. Gauthier, L. Giuffrida, G. D. Glenn, S. H. Glenzer, J. S. Green, R. J. Gray, G. S. Hicks, C. Hyland, V. Istokskaia, M. King, D. Margarone, O. McCusker, P. McKenna, Z. Najmudin, C. Parisuaña, P. Parsons, C. Spindloe, D. R. Symes, A. G. R. Thomas, F. Treffert, N. Xu, and C. A. J. Palmer, High Power Laser Sci. Eng. **11**, e35 (2023).
15. F. Nürnberg, M. Schollmeier, E. Brambrink, A. Blaževi'c, D. C. Carroll, K. Flippo, D. C. Gautier, M. Geißel, K. Harres, B. M. Hegelich, O. Lundh, K. Markey, P. McKenna, D. Neely, J. Schreiber, and M. Roth, Rev. Sci. Instrum. **80**, 033301 (2009).
16. M. S. Schollmeier, *Optimization and Control of Laser-Accelerated Proton Beams*, PhD Thesis (Technische Universität Darmstadt, 2009).
17. D. Carroll, *Laser Driven Ion Acceleration: Source Optimisation and Optical Control*, PhD Thesis (University of Strathclyde, 2008).
18. F. Consoli, V. T. Tikhonchuk, M. Bardon, P. Bradford, D. C. Carroll, J. Cikhardt, M. Cipriani, R. J. Clarke, T. E. Cowan, C. N. Danson, R. De Angelis, M. De Marco, J.-L. Dubois, B. Etchessahar, A. L. Garcia, D. I. Hillier, A. Honsa, W. Jiang, V. Kmetik, J. Krása, Y. Li, F. Lubrano, P. McKenna, J. Metzkes-Ng, A. Poyé, I. Prencipe, P. Raczka, R. A. Smith, R. Vrana, N. C. Woolsey, E. Zemaityte, Y. Zhang, Z. Zhang, B. Zielbauer, and D. Neely, High Power Laser Sci. Eng. **8**, e22 (2020).
19. P. Lecoq, *Scintillation Detectors for Charged Particles and Photons* (Springer International Publishing, Cham, 2020), p. 45.
20. L. Gruber and LHCb SciFi Tracker Collaboration, Nucl. Instrum. Methods Phys. Res. Sect. A **958**, 162025 (2020).
21. P. R. Bolton, M. Borghesi, C. Brenner, D. C. Carroll, C. De Martinis, F. Fiorini, A. Flacco, V. Floquet, J. Fuchs, P. Gallegos, D. Giove, J. S. Green, S. Green, B. Jones, D. Kirby, P. McKenna, D. Neely, F. Nuesslin, R. Prasad, S. Reinhardt, M. Roth, U. Schramm, G. G. Scott, S. Ter-Avetisyan, M. Tolley, G. Turchetti, and J. J. Wilkens, Phys. Medica **30**, 255 (2014).
22. J. D. Kilkenny, W. W. Hsing, S. H. Batha, G. A. Rochau, T. C. Sangster, P. M. Bell, D. K. Bradley, H. Chen, J. A. Frenje, M. Gatu-Johnson, V. Yu. Glebov, R. J. Leeper, A. J. Mackinnon, S. P. Regan, J. S. Ross, and J. l. Weaver, Rev. Sci. Instrum. **94**, 081101 (2023).
23. J. S. Green, M. Borghesi, C. M. Brenner, D. C. Carroll, N. P. Dover, P. S. Foster, P. Gallegos, S. Green, D. Kirby, K. J. Kirkby, P. McKenna, M. J. Merchant, Z. Najmudin, C. A. J. Palmer, D. Parker, R. Prasad, K. E. Quinn, P. P. Rajeev, M. P. Read, L. Romagnani, J. Schreiber, M. J. V. Streeter, O. Tresca, C.-G. Wahlström, M. Zepf, and D. Neely, Proc. SPIE **8079**, 807919 (2011).
24. M. Huault, D. De Luis, J. I. Apiñaniz, M. De Marco, C. Salgado, N. Gordillo, C. G. Neira, J. A. Pérez-Hernández, R. Fedosejevs, G. Gatti, and L. Volpe, High Power Laser Sci. Eng. **7**, e60 (2019).
25. J. Metzkes, K. Zeil, S. D. Kraft, L. Karsch, M. Sobiella, M. Rehwald, L. Obst, H.-P. Schlenvoigt, and U. Schramm, Rev. Sci. Instrum. **87**, 083310 (2016).
26. N. P. Dover, M. Nishiuchi, H. Sakaki, M. A. Alkhimova, A. Y. Faenov, Y. Fukuda, H. Kiriyama, A. Kon, K. Kondo, K. Nishitani, K. Ogura, T. A. Pikuz, A. S. Pirozhkov, A. Sagisaka, M. Kando, and K. Kondo, Rev. Sci. Instrum. **88**, 073304 (2017).
27. N. P. Dover, M. Nishiuchi, H. Sakaki, K. Kondo, H. F. Lowe, M. A. Alkhimova, E. J. Ditter, O. C. Ettlinger, A. Y. Faenov, M. Hata, G. S. Hicks, N. Iwata, H. Kiriyama, J. K. Koga, T. Miyahara, Z. Najmudin, T. A. Pikuz, A. S. Pirozhkov, A. Sagisaka, U. Schramm, Y. Sentoku, Y. Watanabe, T. Ziegler, K. Zeil, M. Kando, and K. Kondo, High Energy Density Phys. **37**, 100847 (2020).
28. D. A. Mariscal, B. Z. Djordjevíc, E. S. Grace, R. Hollinger, T. Ma, G. G. Scott, H. Song, R. A. Simpson, J. J. Rocca, and S. Wang, Plasma Phys. Controll. Fusion **63**, 114003 (2021).
29. M. Hesse, T. Ebert, M. Zimmer, S. Scheuren, G. Schaumann, and M. Roth, Rev. Sci. Instrum. **92**, 093302 (2021).
30. A. B. Zylstra, C. K. Li, H. G. Rinderknecht, F. H. Sèguin, R. D. Petrasso, C. Stoeckl, D. D. Meyerhofer, P. Nilson, T. C. Sangster, S. Le Pape, A. Mackinnon, and P. Patel, Rev. Sci. Instrum. **83**, 013511 (2012).
31. R. A. Simpson, D. A. Mariscal, J. Kim, N. Lemos, E. S. Grace, K. K. Swanson, G. G. Scott, B. Z. Djordjevic, and T. Ma, Phys. Plasmas **30**, 103103 (2023).
32. C. M. Huntington, F. Fiuza, J. S. Ross, A. B. Zylstra, R. P. Drake, D. H. Froula, G. Gregori, N. L. Kugland, C. C. Kuranz, M. C. Levy, C. K. Li, J. Meinecke, T. Morita, R. Petrasso, C. Plechaty, B. A. Remington, D. D. Ryutov, Y. Sakawa, A. Spitkovsky, H. Takabe, and H.-S. Park, Nat. Phys. **11**, 173 (2015).
33. P. Tzeferacos, A. Rigby, A. F. A. Bott, A. R. Bell, R. Bingham, A. Casner, F. Cattaneo, E. M. Churazov, J. Emig, F. Fiuza, C. Graziani, J. Katz, M. Koenig, C.-K. Li, J. Meinecke, R. Petrasso, H.-S. Park, B. A. Remington, J. S. Ross, D. Ryu, D. Ryutov, T. G. White, B. Reville, F. Miniati, A. A. Schekochihin, D. Q. Lamb, D. H. Froula, C. B. Forest, J. Foster, and G. Gregori, Nat. Commun. **9**, 591 (2018).
34. M. Borghesi, D. H. Campbell, A. Schiavi, M. G. Haines, O. Willi, A. J. MacKinnon, P. Patel, L. A. Gizzi, M. Galimberti, R. J. Clarke, F. Pegoraro, H. Ruhl, and S. Bulanov, Phys. Plasmas **9**, 2214 (2002).
35. M. Reimold, S. Assenbaum, E. Beyreuther, E. Bodenstein, F.-E. Brack, C. Eisenmann, F. Englbrecht, F. Kroll, F. Lindner, U. Masood, J. Pawelke, U. Schramm, M. Schneider, M. Sobiella, M. E. P. Umlandt, M. Vescovi, K. Zeil, T. Ziegler, and J. Metzkes-Ng, High Power Laser Sci. Eng. **11**, e68 (2023).
36. A. Corvino, M. Reimold, E. Beyreuther, F.-E. Brack, F. Kroll, J. Pawelke, J. D. Schilz, M. Schneider, U. Schramm, M. E. P. Umlandt, K. Zeil, T. Ziegler, and J. Metzkes-Ng, High Power Laser Sci. Eng. **12**, e17 (2024).
37. J. Esteves, O. Pivot, J. Ribouton, P. Jalade, A. Zouaoui, L. Desbat, S. Rit, F. Blanc, G. Haefeli, P. Hopchev, J.-M. Galvan, G.-N. Lu, and P. Pittet, Med. Phys. **50**, 619 (2023).
38. S. Agostinelli, J. Allison, K. Amako, J. Apostolakis, H. Araujo, P. Arce, M. Asai, D. Axen, S. Banerjee, G. Barrand, F. Behner, L. Bellagamba, J. Boudreau, L. Broglia, A. Brunengo, H. Burkhardt, S. Chauvie, J. Chuma, R. Chytracek, G. Cooperman, G. Cosmo, P. Degtyarenko, A. Dell'Acqua, G. Depaola, D. Dietrich, R. Enami, A. Feliciello, C. Ferguson, H. Fesefeldt, G. Folger, F. Foppiano, A. Forti, S. Garelli, S. Giani, R. Giannitrapani, D. Gibin, J. J. Gómez Cadenas, I. González, G. Gracia Abril, G. Greeniaus, W. Greiner, V. Grichine, A. Grossheim, S. Guatelli, P. Gumplinger, R. Hamatsu, K. Hashimoto, H. Hasui, A. Heikkinen, A. Howard, V. Ivanchenko, A. Johnson, F. W. Jones, J. Kallenbach, N. Kanaya, M. Kawabata, Y. Kawabata, M. Kawaguti, S. Kelner, P. Kent, A. Kimura, T. Kodama, R. Kokoulin, M. Kossov, H. Kurashige, E. Lamanna, T. Lampén, V. Lara, V. Lefebure, F. Lei, M. Liendl, W. Lockman, F. Longo, S. Magni, M. Maire,

https://doi.org/10.1017/hpl.2024.62 Published online by Cambridge University Press

E. Medernach, K. Minamimoto, P. Mora de Freitas, Y. Morita, K. Murakami, M. Nagamatu, R. Nartallo, P. Nieminen, T. Nishimura, K. Ohtsubo, M. Okamura, S. O'Neale, Y. Oohata, K. Paech, J. Perl, A. Pfeiffer, M. G. Pia, F. Ranjard, A. Rybin, S. Sadilov, E. Di Salvo, G. Santin, T. Sasaki, N. Savvas, Y. Sawada, S. Scherer, S. Sei, V. Sirotenko, D. Smith, N. Starkov, H. Stoecker, J. Sulkimo, M. Takahata, S. Tanaka, E. Tcherniaev, E. Safai Tehrani, M. Tropeano, P. Truscott, H. Uno, L. Urban, P. Urban, M. Verderi, A. Walkden, W. Wander, H. Weber, J. P. Wellisch, T. Wenaus, D. C. Williams, D. Wright, T. Yamada, H. Yoshida, and D. Zschiesche, Nucl. Instrum. Methods Phys. Res. Sect. A **506**, 250 (2003).

39. F. E. Merrill, D. Bower, R. Buckles, D. D. Clark, C. R. Danly, O. B. Drury, J. M. Dzenitis, V. E. Fatherley, D. N. Fittinghoff, R. Gallegos, G. P. Grim, N. Guler, E. N. Loomis, S. Lutz, R. M. Malone, D. D. Martinson, D. Mares, D. J. Morley, G. L. Morgan, J. A. Oertel, I. L. Tregillis, P. L. Volegov, P. B. Weiss, C. H. Wilde, and D. C. Wilson, Rev. Sci. Instrum. **83**, 10D317 (2012).
40. B. D. Leverington, M. Dziewiecki, L. Renner, and R. Runze, J. Instrum. **13**, P05030 (2018).
41. J. B. Birks, Proc. Phys. Soc. Sect. A **64**, 874 (1951).
42. S. Tong, A. M. Alessio, and P. E. Kinahan, Imaging Med. **2**, 529 (2010).
43. S. Richard, D. B. Husarik, G. Yadava, S. N. Murphy, and E. Samei, Med. Phys. **39**, 4115 (2012).
44. R. A. Brooks and G. Di Chiro, Phys. Med. Biol. **21**, 689 (1976).
45. S. J. Glick, M. A. King, and B. C. Penney, IEEE Trans. Med. Imaging **8**, 203 (1989).
46. D. Y. Li, X. H. Xu, T. Yang, M. J. Wu, Y. F. Zhang, H. Cheng, X. Y. Hu, Y. X. Geng, J. G. Zhu, Y. Y. Zhao, K. Zhu, W. J. Ma, C. Lin, and X. Q. Yan, AIP Adv. **11**, 085316 (2021).
47. J. F. Ziegler, M. D. Ziegler, and J. P. Biersack, Nucl. Instrum. Methods Phys. Res. B **268**, 1818 (2010).
48. C. Angelini, W. Beusch, A. Cardini, D. J. Crennell, M. De Vincenzi, G. Di Vita, A. Duane, J.-P. Fabre, V. Flaminio, A. Frenkel, T. Gys, K. Harrison, E. Lamanna, H. Leutz, D. Lucchesi, G. Martellotti, J. G. McEwen, D. R. O. Morrison, G. Penso, S. Petrera, C. Roda, A. Sciubba, E. Vicari, and D. M. Websdale, Nucl. Instrum. Methods Phys. Res. A **295**, 299 (1990).
49. C. D'Ambrosio, H. Leutz, T. Shimizu, and O. Shinji, Nucl. Instrum. Methods Phys. Res. Sect. A **325**, 161 (1993).
50. A. Ichikawa, S. Aoki, K. Imai, M. Kaneko, Y. Kondo, K. Nakazawa, H. Tanaka, K. Yamamoto, and T. Yoshida, Nucl. Instrum. Methods Phys. Res. Sect. A **417**, 220 (1998).
51. https://www.mi-net.co.uk/product/scintillating-fiber/.
52. M. Schollmeier, M. Geissel, A. B. Sefkow, and K. A. Flippo, Rev. Sci. Instrum. **85**, 043305 (2014).
53. https://www.kuraray.com/products/psf.
54. C. Penner, S. Usherovich, J. Niedermeier, C. Belanger-Champagne, M. Trinczek, E. Paulssen, and C. Hoehr, Electronics **12**, 11 (2023).
55. https://www.thorlabs.com/thorproduct.cfm?partnumber=FT1000UMT.
56. Z. Major, U. Eisenbarth, B. Zielbauer, C. Brabetz, J. B. Ohland, Y. Zobus, S. Roeder, D. Reemts, S. Kunzer, S. Götte, D. Neidherr, J. Hornung, P. Kewes, D. Schumacher, D. Beck, P. Hesselbach, M. Malki, P. Neumayer, K. Weyrich, A. Tauschwitz, and V. Bagnoud, High Power Laser Sci. Eng. **12**, e39 (2024).
57. S. M. Wiggins, M. Boyd, E. Brunetti, N. M. H. Butler, J. S. Feehan, R. J. Gray, B. Hidding, D. G. Ireland, W. Li, A Maitrallain, G. G. Manahan, P. McKenna, D. O'Donnell, M. Scheck, M. Shahzad, Z.-M. Sheng, R. Spesyvtsev, G. Vieux, D. P. Watts, G. H. Welsh, R. Wilson, N. Zachariou, and D. A. Jaroszynski, Proc. SPIE **11036**, 110360T (2019).
58. https://www.alliedvision.com/en/camera-selector/detail/manta/g-235/.
59. P. Dervan, R. French, P. Hodgson, H. Marin-Reyes, and J. Wilson, Nucl. Instrum. Methods Phys. Res. Sect. A **730**, 101 (2013).
60. P. Mora, Phys. Rev. Lett. **90**, 185002 (2003).
61. J. Fuchs, P. Antici, E. d'Humières, E. Lefebvre, M. Borghesi, E. Brambrink, C. A. Cecchetti, M. Kaluza, V. Malka, M. Manclossi, S. Meyroneinc, P. Mora, J. Schreiber, T. Toncian, H. Pépin, and P. Audebert, Nat. Phys. **2**, 48 (2006).
62. M. G. Haines, M. S. Wei, F. N. Beg, and R. B. Stephens, Phys. Rev. Lett. **102**, 045008 (2009).
63. S. C. Wilks, W. L. Kruer, M. Tabak, and A. B. Langdon, Phys. Rev. Lett. **69**, 1383 (1992).
64. L. A. Shepp and Y. Vardi, IEEE Trans. Med. Imaging **1**, 113 (1982).
65. B. T. Spiers, R. Aboushelbaya, Q. Feng, M. W. Mayr, I. Ouatu, R. W. Paddock, R. Timmis, R. H.-W. Wang, and P. A. Norreys, Phys. Rev. E **104**, 045201 (2021).
66. G. S. Hicks, N. P. Dover, R. Nichols, P. Posocco, Z. Najmudin, and J. S. Green, "Proton spectra calculation from radiochromic film stacks with high-energy proton correction," Technical report (Central Laser Facility, 2013).
67. E. Breschi, M. Borghesi, M. Galimberti, D. Giulietti, L. A. Gizzi, and L. Romagnani, Nucl. Instrum. Methods Phys. Res. Sect. A **522**, 190 (2004).
68. E. Esarey, B. A. Shadwick, P. Catravas, and W. P. Leemans, Phys. Rev. E **65**, 056505 (2002).
69. H. Schwoerer, B. Liesfeld, H.-P. Schlenvoigt, K.-U. Amthor, and R. Sauerbrey, Phys. Rev. Lett. **96**, 014802 (2006).
70. K. T. Phuoc, S. Corde, C. Thaury, V. Malka, A. Tafzi, J.-P. Goddet, R. C. Shah, S. Sebban, and A. Rousse, Nat. Photonics **6**, 308 (2012).
71. S. Chen, N. D. Powers, I. Ghebregziabher, C. M. Maharjan, C. Liu, G. Golovin, S. Banerjee, J. Zhang, N. Cunningham, A. Moorti, S. Clarke, S. Pozzi, and D. P. Umstadter, Phys. Rev. Lett. **110**, 155003 (2013).
72. D. R. Rusby, C. D. Armstrong, C. M. Brenner, R. J. Clarke, P. McKenna, and D. Neely, Rev. Sci. Instrum. **89**, 073502 (2018).
73. C.-S. Wong, J. Strehlow, D. P. Broughton, S. V. Luedtke, C.-K. Huang, A. Bogale, R. Fitzgarrald, R. Nedbailo, J. L. Schmidt, T. R. Schmidt, J. Twardowski, A. Van Pelt, M. Alvarado-Alvarez, A. Junghans, L. T. Mix, R. E. Reinovsky, D. R. Rusby, Z. Wang, B. Wolfe, B. J. Albright, S. H. Batha, and S. Palaniyappan, Rev. Sci. Instrum. **95**, 023301 (2024).
74. K. T. Behm, J. M. Cole, A. S. Joglekar, E. Gerstmayr, J. C. Wood, C. D. Baird, T. G. Blackburn, M. Duff, C. Harvey, A. Ilderton, S. Kuschel, S. P. D. Mangles, M. Marklund, P. McKenna, C. D. Murphy, Z. Najmudin, K. Poder, C. P. Ridgers, G. Sarri, G. M. Samarin, D. Symes, J. Warwick, M. Zepf, K. Krushelnick, and A. G. R. Thomas, Rev. Sci. Instrum. **89**, 113303 (2018).
75. C. D. Armstrong, D. Neely, D. Kumar, P. McKenna, R. J. Gray, and A. S. Pirozhkov, Rev. Sci. Instrum. **92**, 113102 (2021).
76. https://andor.oxinst.com/products/scientific-cmos-emccd-and-ccd-research-cameras.
77. B. Schmitz, M. Metternich, and O. Boine-Frankenheim, Rev. Sci. Instrum. **93**, 093306 (2022).

https://doi.org/10.1017/hpl.2024.62 Published online by Cambridge University Press